

# Progress towards a 3D Monte Carlo radiative transfer code for outflow wind modelling

## II. 3-D applications

J. Fišák<sup>1</sup>, J. Kubát<sup>1</sup>, N. Moens<sup>2</sup>, and B. Kubátová<sup>1</sup>

<sup>1</sup> Astronomical Institute of the Czech Academy of Sciences, Fričova 298, CZ-251 65, Ondřejov, Czech Republic  
e-mail: jakub.fisak@asu.cas.cz

<sup>2</sup> Instituut voor Sterrenkunde, KU Leuven, Celestijnenlaan 200D, 3001 Leuven, Belgium

January 30, 2026

### ABSTRACT

**Context.** The massive hot stars play crucial role in the dynamics of galaxies. These stars influence their surroundings through strong winds which are highly structured processes. The theoretical study of the non-symmetric phenomena of the stellar winds are becoming important these days, mainly because 1-D models are not sufficient enough.

**Aims.** We present a new version of our Monte Carlo radiative transfer code “Andy Antares” with improved treatment of the velocity field for arbitrary geometries. Our aim is to develop a numerical scheme that can incorporate a general velocity field defined at discrete points. Our main objective is to calculate radiative transfer in a general input hydrodynamic model.

**Methods.** The “Andy Antares” code currently calculates pure radiative transfer. The input model is pre-calculated by another hydrodynamical code. The whole radiative transfer calculation is then processed in a Cartesian grid. Radiative transfer is solved using the Monte Carlo approach in 3-D regardless of the input hydrodynamical model’s dimension. The velocity field at any given point is interpolated using the trilinear interpolation. The optical depth is then integrated numerically along the photon’s path.

**Results.** We verified the accuracy of the numerical velocity interpolation by comparison with results obtained for analytical velocity fields, achieving successful outcomes. We also tested the radiative transfer solution on a 3-D model generated from a 2-D hydrodynamic model, and obtained emergent radiation.

**Conclusions.** The code is suitable for the numerical solution of radiative transfer in 3-D with arbitrary velocity fields.

**Key words.** stars: atmospheres – stars: winds, outflows – radiative transfer – methods: numerical

## 1. Introduction

Radiatively driven outflows from massive hot stars (O, B, and Wolf-Rayet stars) are a cornerstone of stellar and galactic evolution. By removing angular momentum and large amounts of mass, these winds reshape surface abundances, alter evolutionary tracks, and regulate feedback into the interstellar medium—thereby influencing everything from local H II regions to the high-redshift ionizing budget. To interpret today’s high-quality UV, optical, and X-ray observations, we need reliable radiative-transfer models of massive-star winds. The mass loss from hot-star winds is crucial to massive-star evolution, yet standard 1-D analyses can misestimate it because real winds are highly structured—densely clumped and porous in space and velocity, and sometimes shaped by magnetic/rotational geometry—which modifies ionization and line formation; consequently, developing genuinely 3-D radiative-transfer (RT) models is now essential for robust diagnostics.

Over the last few years, theory has increasingly shown that 1-D hot-star atmosphere/wind analyses are inadequate because rotation, magnetic confinement, corotating interaction regions, and small-scale clumping/vorosity make the outflows intrinsically 3-D—pushing us toward full 3-D RT models for trustworthy mass-loss diagnostics. The Moens et al. (2022a,b) illustrates the origin of clumps in the atmospheres. The 2-D models were studied by Debnath et al. (2024). Later, ud-Doula et al. (2025)

and Narechania et al. (2025) showed numerically that magnetic fields indeed also can affect structure formations in these multi-D setups. Hot stars are studied also in the ULLYSES project, such as Sander et al. (2024).

The standard 1-D spectral synthesis codes such as FASTWIND, CMFGEN, PoWR, ... treat velocity field with several crucial assumptions. The main approximation is an exclusion of non-monotonical velocity fields. Treatment of general velocity field is significantly more complicated. Many codes, such as Tardis (Kerzendorf & Sim 2014; Vogl et al. 2019; Kerzendorf et al. 2022), the SIROCCO (formerly Python) code (Matthews et al. 2025; Long & Knigge 2002, and Higginbottom et al. 2013), Monte Carlo clumping wind model (Šurlan et al. 2012, 2013), the PoWR code (Gräfener et al. 2002; Hamann & Gräfener 2003; Sander et al. 2015) use analytical velocity fields. Analytical velocity fields are simpler to treat than numerical ones because the latter require interpolation procedures to be implemented. The non-analytical solutions are possible in the SIROCCO (formerly Python) code mentioned earlier.

In this paper, we build on the work presented in our previous paper (Fišák et al. 2023, hereafter Paper I), in which the Monte Carlo code “Andy Antares”<sup>1</sup> had been introduced.

<sup>1</sup> This code is available online <https://github.com/jfisak/andyAntares>

We show some first applications on the first full 3-D models and we will describe important differences between 1-D and multi-D cases. In Section 2 we describe all used methods and calculations. Section 3 shows tests of simple 1-D models solved using algorithms applicable to general 3-D problems. Finally, in Section 4 we present the very first applications on full 3-D (2-D) models including calculation of angle dependent spectra.

## 2. Methods

The code uses two basic grids, the model grid (hereafter modGrid), and the propagation grid (hereafter propGrid). The modGrid describes the underlying hydrodynamic model atmosphere structure (e.g. temperature, density, velocity, etc.) and may use any coordinates (cartesian, spherical polar, cylindrical, etc.). The propGrid is used for radiation transfer and uses exclusively the cartesian coordinates. Relation between these two grids is described in detail in Paper I. Hereafter, we define a ‘modGrid cell’ as a volume in 3-D space containing a point defined in the input file. In the 1-D case, it can be a spherical shell, and in 2-D and 3-D cases, it can be a more complicated shape. The propGrid cell is always a cube-shaped volume.

### 2.1. Treatment of interaction in lines

All considered atomic lines are stored in a single array. For each line, this array contains atomic ion information (element index, ion index, lower and upper level indexes), the line frequency, and the oscillator strength. A packet will interact with the line(s) closest to the CMF frequency of the packet if the condition (13) in Paper I is met – their resonance (Sobolev) points ( $v^{\rightarrow} = v_{\text{line}}$ ) are the closest to the packet’s current position. We assume that the velocity field changes smoothly between model points, so the CMF frequency also changes smoothly.

The most effective way is to sort the line list in respect to the line frequency. If we calculate the CMF frequency of a packet and if the frequency is an increasing or decreasing function along the packet’s path, we can find the next (and the closest) line the packet will interact with. This is followed by incrementing/decrementing of an index of the next line, instead of searching in an unsorted array, which significantly saves a lot of computing time.

Another advantage of using the described method is a straightforward application to non-monotonic velocity fields. Using one logical variable detecting if the CMF frequency of a packet is increasing or decreasing, we can simply select the correct line in the corresponding blue or red shift. This possibility is an advantage of our code because other codes either do not include blue shifted parts properly or omit them completely.

### 2.2. Diagnostics of created propGrid

The created propGrid is crucial for a proper description of the whole model. Consequently, it must be tested, if the propGrid correctly covers the physical model (represented by the modGrid) and if all inhomogeneities are included in the calculation via the propGrid as well. In this section, we describe the methods used to test the created propGrid.

Some tests have already been published in Paper I in Section 4. Firstly we check, if all modGrid cells are connected to at least one propGrid cell. This is called “Relative covering” in the paper Paper I (see Table 3 in that paper). This number should be equal to one.

The second method compares volumes of propGrid cells and connected modGrid cells: the first equation (Eq. 41 and 42 in Paper I),

$$\chi_I = \frac{\sum_{\text{PC} \rightarrow I} V_{\text{PC}}}{V_I}, \quad (\text{I.41})$$

describes the ratio of the volumes of all propGrid cells PC associated with modGrid  $I$  to the total volume of modGrid I:  $V_I$ . To make the results more clear, we calculated the standard deviation of all modGrid cells using Eq. (42) from Paper I,

$$\sqrt{\langle \chi^2 \rangle} = \sqrt{\frac{1}{N_{\text{modGrid}}} \sum_{I=1}^{N_{\text{modGrid}}} (\chi_I - 1)^2}, \quad (\text{I.42})$$

which should equal zero in an ideal case.

We used the relative covering test to check the created grid. The second method is really tricky to calculate in 2-D and 3-D cases, since we have to calculate the Voronoi volumes for each point in multidimensional space. This calculation will therefore be added in the future.

### 2.3. Velocity field treatment

Most 3-D hydrodynamic codes also provide full information about the velocity structure, consequently, each grid point in modGrid contains a velocity vector. When solving radiative transfer in a moving environment, we need to obtain a velocity vector generally at any given point. This is not an easy procedure, hence we have developed an algorithm based on the trilinear interpolation method.

A simple approximation of the velocity field via a step function (i.e. constant velocity within a given propGrid cell) is not acceptable. This can lead to the incorrect treatment of line and continuum interactions since the continuum optical depth depends on the path length over which interaction is possible. The Doppler shift (hence the CMF frequency) has to be known exactly at each point along the packet’s trajectory. The position of the resonance points is important for the determination of packet interactions with matter. If the velocity field were described by an analytical function (as, for example, in Paper I), the computation would be quite simple. However, the general input velocity field can not be approximated by a simple analytical function. Therefore, an interpolation technique must be implemented in the code.

We used a method which obtains velocity vectors from connected modGrid cells during photon propagation. This method is described in detail in the forthcoming paragraphs.

#### 2.3.1. Interpolation of the velocity field from the modGrid

The method is illustrated at Fig. 1. It gets the velocity vector directly from the modGrid associated with the propGrid cell in question during packet propagation. First of all, the interpolation points (the blue and red hexagons in the upper part of Fig. 1) are obtained. These points mark the corners of a cell of the same size as the current propGrid cell, with the blue hexagon corner at the current propGrid cell centre. The corners are positioned so that the dark star (the place where we calculate the interpolated velocity vector) is inside the created object, which is marked by an orange dashed line. The velocity vectors of the propGrid cells are

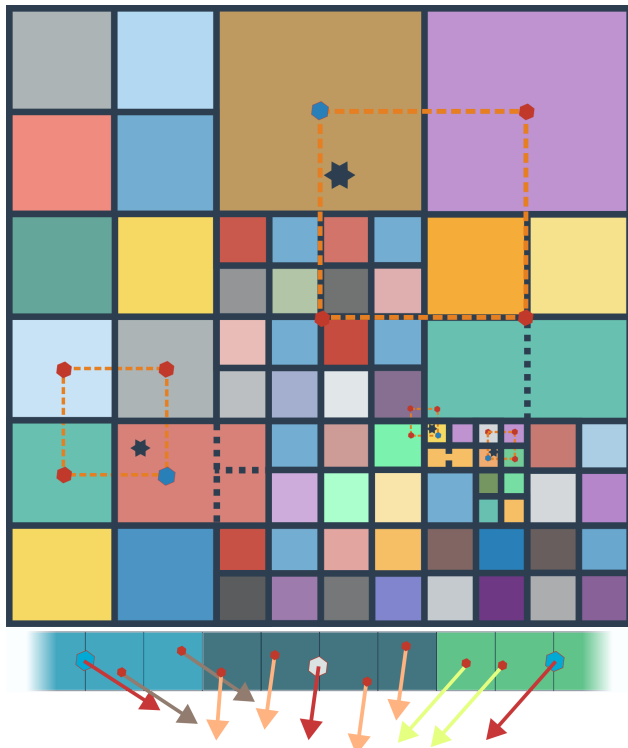


**Fig. 1.** An illustrative example of an adaptive propGrid with propGrid cells belonging to different modGrid cells. Each propGrid cell belongs to any modGrid cell, which is distinguished by different colours (the same colour of non-neighbouring cells does not mean the same associated modGrid cell, we did not want to use many colours). *Above:* An algorithm for choosing interpolation points based on the current propGrid cell. The current propGrid cell is the cell containing a dark star, which locates the place where we calculate the interpolated velocity vector. There are four such examples in the figure. The blue hexagons represent the central points of the current propGrid cells (where the dark stars are located), the red hexagons represent the derived points used for the trilinear interpolation. If more than one propGrid cell belongs to the same modGrid cell, the boundary between them is drawn with a dotted line. *Below:* The red arrows represent the velocity vectors defined in the input. The other arrows represent the velocity vectors used for trilinear interpolation at any particular point (in this picture represented by little red hexagons).

defined as those of the corresponding modGrid cells and are defined at each corner of the orange cube (red hexagons). This velocity is the same as the velocity of the modGrid cell belonging to the given propGrid cell (distinguished by the different colours of the propGrid cells). As can be seen from Fig. 1 below, if more propGrid cells belong to one modGrid cell, the velocity vector is the same in all of these propGrid cells.<sup>2</sup>

#### 2.4. Line interaction calculation

The interaction in lines, or better said, the line optical depth calculation, changes in the case of a more general velocity field. We cannot use the simple equation (Paper I, Eq. 10) for these, because it is only valid for spherically symmetric velocity fields. Instead, we have to use the more general equation (still assuming

<sup>2</sup> This only applies to the 3-D model. For the 1-D and 2-D models, the vector magnitudes are the same, but the direction differs depending on the position, for example in the case of a radial field.

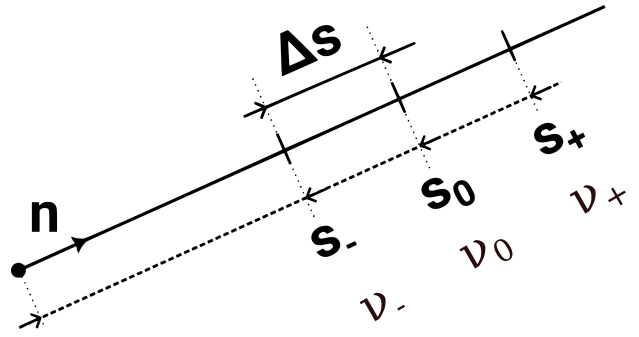


**Fig. 2.** The derivative  $ds/dv^{\sim}$  is calculated using Eq. 1. A packet is located in the beginning of the dashed line, the arrow points to its current direction. The resonance point is denoted by  $s_0$  and the packet's CMF frequency is exactly equal to the line frequency.  $s_-$  and  $s_+$  denote positions of points with a distance  $\Delta s$  from the resonance point.

the Sobolev approximation), which is of the form

$$\tau_{\text{line}} = n_l f_{lu} \frac{\pi e^2}{m_e c} \left( 1 - \frac{n_u g_l}{n_l g_u} \right) \times \left( \frac{ds}{dv^{\sim}} \right)_{v_{lu}} \times \begin{cases} 0 & v_{lu} \notin [v^{\sim}(0), v^{\sim}(s_0)] \\ -1 & v_{lu} \in [v^{\sim}(0), v^{\sim}(s_0)] \end{cases} \quad (1)$$

here (cf. Eq. (9) in Paper I or Eq. 4.15 in Kromer 2009, where the Einstein coefficient  $B_{lu}$  instead of the oscillator strength  $f_{lu}$  is used). The indexes  $l$  and  $u$  denote the lower and upper energy level, respectively;  $n_l$  and  $n_u$  denote the respective level populations,  $g_l$ ,  $g_u$  are the statistical weights,  $B_{lu}$  is the Einstein B coefficient,  $v_{lu}$  is the transition frequency between these two levels. Finally,  $s$  measures the distance from the current position (geometrically, it is a line parameter), and  $s_0$  denotes the position of the resonance point.

From Eq. (1) it is clear that the derivative  $ds/dv^{\sim}$  must be evaluated, which introduces several additional numerical problems to solve. One of the problems is the choice of appropriate  $\Delta s$ , since at least two points are needed to calculate a derivative. Its value at the point  $s_0$  is

$$\left( \frac{ds}{dv^{\sim}} \right)_{v_{lu}} = \frac{s_+ - s_-}{v_+ - v_-}, \quad (2)$$

in the case, when  $s_0 - s_- = s_+ - s_0 = \Delta s$  (the resonance point is located exactly in the middle of points  $s_+$  and  $s_-$ , see Fig. 2).

### 3. Testing the generalized 3-D calculations

The MC calculations are processed in a 3-D space, however, the equations implemented in Paper I assume spherical symmetry of the models. Here we generalise these equations for a 3-D calculation. We test these new 3-D algorithms on spherically symmetric cases and compare the results with calculations of the same models in 1-D.

In order to test the properties of 3-D radiation transfer in more detail, and to avoid being overwhelmed by the possible difficulties of a general modGrid, we use a regularly spaced modGrid. This enables us to create the propGrid so that each of its cells contains one modGrid cell.

We show simple tests of 3-D procedures. The key factor is the velocity interpolation, which is described in the next section. In the subsequent section we test the calculation of the line optical depth which is more complex in the case of 3-D models.

parameter	value
effective temperature $T_{\text{eff}}$	14734 K
stellar radius $R_*$	$8072 R_{\odot}$
upper boundary $R_{\infty}$	$5 R_*$
outer boundary velocity $V_{\infty}$	$3 \times 10^9 \text{ cm} \cdot \text{s}^{-1}$
$\beta$ parameter	1.3
$N_x \times N_y \times N_z$ (homologous)	$50 \times 50 \times 50$
$N_x \times N_y \times N_z$ (beta-law)	$200 \times 200 \times 200$
range of the propGrid (same for $x, y$ , and $z$ )	$(-5.1 \cdot R_*, +5.1 \cdot R_*)$
propGrid cell width (same for $x, y$ , and $z$ ) (homologous)	$\frac{1}{5} R_*$
propGrid cell width (same for $x, y$ , and $z$ ) (beta-law)	$\frac{1}{20} R_*$
number of packets	20000000

**Table 1.** Parameters for the calculated models. The upper part shows the general setup of the computational domain, and the physical conditions at the boundaries. The middle part shows the properties of the regular propGrid, and the bottom part specifies the number of packets used in the calculation.

### 3.1. Velocity field

In this part, we apply the method described in the Section 2.3, and test the interpolation method 2.3.1. We ran several simple tests to evaluate the implementation of trilinear interpolation. The first of these compares the analytical and numerically calculated velocity magnitudes. For this purpose, we created a simple 3-D model, its parameters are described in Tab. 1. In this model, each modGrid cell position is defined by a vector  $\mathbf{r}$  with three independent coordinates,  $x, y$ , and  $z$ , namely

$$\mathbf{r} = \mathbf{r}_{\min} + (i \cdot w_x, j \cdot w_y, k \cdot w_z), \quad (3)$$

where the indexes  $(i, j, k)$  are integers from the set  $\{1, 2, \dots, N_d\}$ ,  $d$  stands for  $x, y$ , or  $z$ .  $N_d$  is defined by the input model  $N_x \times N_y \times N_z$ , and

$$\mathbf{r}_{\min} = (x_{\min}, y_{\min}, z_{\min}) \quad (4)$$

are the coordinates of the modGrid corner ( $x_{\min}, y_{\min}$ , and  $z_{\min}$  are minimum values of the  $x, y$ , and  $z$  coordinates, respectively). The maximum coordinates of the modGrid are

$$\mathbf{r}_{\max} = \mathbf{r}_{\min} + [(N_x - 1) \cdot w_x, (N_y - 1) \cdot w_y, (N_z - 1) \cdot w_z], \quad (5)$$

where  $\mathbf{w} = (w_x, w_y, w_z)$  is the distance between points in all three directions, simply calculated from the total size of the modGrid and the number of cells in a selected dimension,

$$w_d = \frac{(\mathbf{r}_{\max})_d - (\mathbf{r}_{\min})_d}{N_d - 1},$$

where  $d$  stands for  $x, y, z$ . The velocity in each modGrid cell is calculated using the formula

$$\mathbf{v}(x_I, y_I, z_I) = \mathbf{v}_I \frac{(x_I, y_I, z_I)}{\sqrt{x_I^2 + y_I^2 + z_I^2}}, \quad (6)$$

Here,  $I$  is an index of a modGrid cell  $I \in \{1, 2, \dots, N_{\text{mg}}\}$  (see Paper I, Section 4),  $\mathbf{v}_I$  is the velocity value in the  $I$ -th modGrid cell,  $N_{\text{mg}} = N_x \cdot N_y \cdot N_z$ , and finally,  $x_I, y_I$ , and  $z_I$  are Cartesian coordinates for the modGrid cell with index  $I$ .

The propGrid can be set very simply. The modGrid is regular and we define the propGrid position so that each modGrid cell

is located at the propGrid cell centre. Therefore, each propGrid cell corner can be defined by a relation

$$\mathbf{r}^{\text{PG}} = \mathbf{r}_{\min}^{\text{PG}} + (i \cdot w_x, j \cdot w_y, k \cdot w_z), \quad (7)$$

where  $\mathbf{r}_{\min}^{\text{PG}} = \mathbf{r}_{\min} - \mathbf{w}/2$  (all variables defined by the modGrid) and, as in the previous case,  $(i, j, k)$  are the integers  $\{1, 2, \dots, N_d\}$ . In this case,

$$\mathbf{r}_{\max}^{\text{PG}} = \mathbf{r}_{\min}^{\text{PG}} + [(N_x + 1) \cdot w_x, (N_y + 1) \cdot w_y, (N_z + 1) \cdot w_z], \quad (8)$$

is the vector with the maximal values of coordinates. Note that propGrid is larger than modGrid in this case.

For the testing purposes, we used two velocity fields. The homologous approximation is a simple linear velocity law, whilst the beta law is a more complicated yet still monotonic, function. The main advantage of these functions is offering the possibility of direct comparison of the calculated velocity with that obtained from an analytical function. We show the differences in both cases.

#### 3.1.1. Homologous approximation

In the homologous approximation, the velocity  $\mathbf{v}_I$  in Eq. (6) is given by

$$\mathbf{v}_I = \sqrt{x_I^2 + y_I^2 + z_I^2} \frac{V_{\infty}}{R_{\infty}}. \quad (9)$$

The left panels of Fig. 3 show the analytical velocity in comparison to the numerically calculated velocities (upper figure) and its relative error (lower figure). The values at the majority of points fit the analytical expression well, with the exception of points close to the lower boundary.

#### 3.1.2. $\beta$ -law

The second test was performed using the velocity field defined by the  $\beta$ -law; this law is expressed as

$$\mathbf{v}(r) = V_{\infty} \left(1 - \frac{R_*}{r}\right)^{\beta}, \quad (10)$$

where  $\beta > 0$  is a parameter determining how quickly the wind is accelerated. The velocity field has been sampled in discrete points, see the Eq. (6);  $\mathbf{v}_I$  is clearly equal to

$$\mathbf{v}_I = V_{\infty} \left(1 - \frac{R_*}{\sqrt{x_I^2 + y_I^2 + z_I^2}}\right)^{\beta}, \quad (11)$$

in the modGrid cell with an index  $I$ . The calculations were performed using the value of  $\beta$  listed in the Table 1. The interpolated values and relative errors are shown in the upper right and lower right panels of Fig. 3, respectively. The values are very close to the analytical function, it appears that there is no problem in this case.

### 3.2. Optical depth in lines

The optical depth in the Sobolev approximation for an arbitrary velocity field is calculated with the Eq. (1). However, for velocity fields described in Section 3.1 we can use the simpler expression (Paper I, Eq. (10)). Both expressions will be used to test the accuracy of the numerical expression.

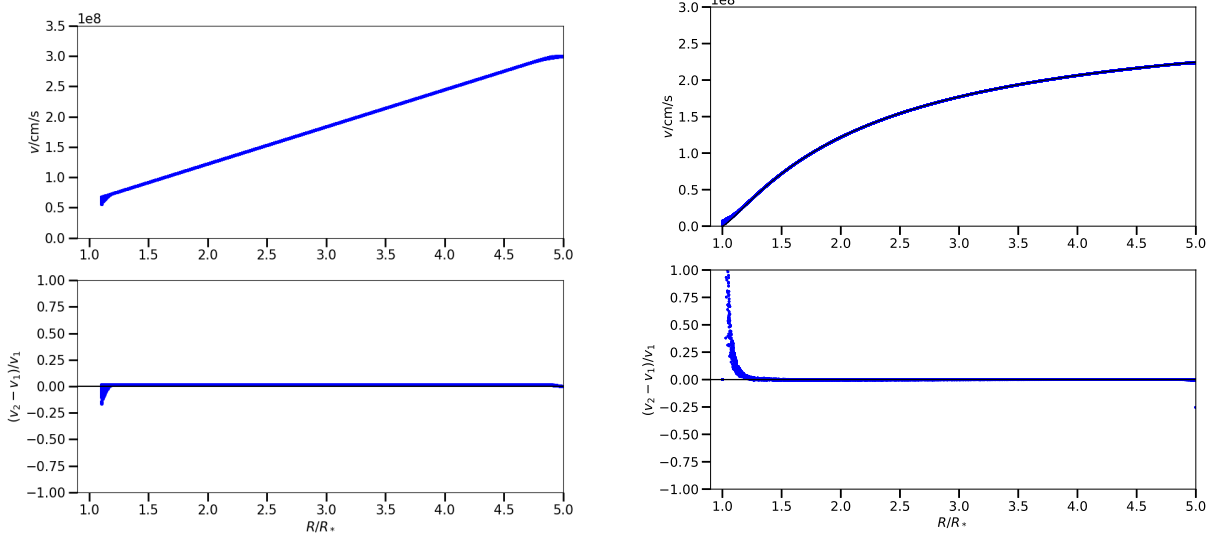


**Fig. 3.** A comparison of the numerical and analytical treatments of velocity, to assess the accuracy of the calculated velocity as a function of radius. The left panels are calculated using the homologous approximation (9) and the right panels are calculated using the  $\beta$ -velocity law (11). The upper panels show the absolute magnitude of the velocity, and the lower panels show the relative difference in velocity magnitudes between the interpolated and analytical values.

We combine equations (10) and (11) from Paper I and write the equation for an optical depth in spherical symmetry in the form

$$\tau_{\text{line}} = \frac{c}{v_{lu}} \mathcal{K} f_{lu} n_l \left( 1 - \frac{n_u}{n_l} \frac{g_l}{g_u} \right) \left[ \mu^2 \frac{dv}{dr} + (1 - \mu^2) \frac{v}{r} \right]^{-1}, \quad (12)$$

here,  $\mathcal{K} = \pi e^2 / (m_e c)$ . In comparison to this equation, Eq. (1) combined with (2) is

$$\tau_{\text{line}} = \mathcal{K} f_{lu} n_l \left( 1 - \frac{n_u g_l}{n_l g_u} \right) \frac{s_+ - s_-}{\sqrt{v_+^2 - v_-^2}}. \quad (13)$$

For a given line, the equations (12) and (13) should give the same value of  $\tau_{\text{line}}$  if the numerical evaluation of (13) is implemented correctly. Accuracy tests were performed on velocity fields calculated using numerical interpolation. 20 000 photon packets were used for evaluation. When a photon packet encountered a line during its passage through the atmosphere, the line's optical depths was calculated using expressions (12) and (13). We refer to these as the 'analytical' and 'numerical' expressions, respectively. These packets meet some line  $N_{\text{points}}$ -times. We calculated a ratio

$$R_\tau = \frac{1}{N_{\text{points}}} \sum_{i=1}^{N_{\text{points}}} \frac{\tau_{i,\text{line}}^{\text{analytical}}}{\tau_{i,\text{line}}^{\text{numerical}}}, \quad (14)$$

which describes the accuracy of numerical calculation of the line optical depth. In the ideal case,  $R_\tau = 1$ . We test the values of  $R_\tau$  for two 1-D velocity fields: a homologous law and a  $\beta$  velocity law.

### 3.2.1. Homologous approximation

For the case of a homologous approximation, the optical depth equation (12) simplifies into the form

$$\tau_{\text{line}} = \frac{c}{v_{lu}} \mathcal{K} f_{lu} n_l \left( 1 - \frac{n_u}{n_l} \frac{g_l}{g_u} \right) \frac{R_{\text{inf}}}{V_{\text{inf}}}. \quad (15)$$

We calculated both values of optical depth using (13) ('numerical') and (15) ('analytical'), the values are equal in the ideal case  $\tau_{i,\text{line}}^{\text{numerical}} = \tau_{i,\text{line}}^{\text{analytical}}$ , however they slightly differ because of numerical uncertainties. In our calculation we got  $R_\tau = 0.959$  for  $N_{\text{points}} = 2932$ , which is a reasonable value.

### 3.2.2. $\beta$ -law

Optical depth in the case of the  $\beta$ -velocity law is simply derivable from the Eq. (12), the optical depth is as follows

$$\tau_{\text{line}} = \frac{c}{v_{lu}} \mathcal{K} f_{lu} n_l \left( 1 - \frac{n_u}{n_l} \frac{g_l}{g_u} \right) \frac{r}{v(r)} \frac{1}{\left[ \mu^2 \left( \frac{R_\tau \beta}{r - R_*} - 1 \right) + 1 \right]}. \quad (16)$$

Here,  $\mu$  is the cosine of the angle between the velocity vector and the direction of the packet, and  $v(r)$  is calculated using Eq. (10). For the  $\beta$ -velocity law we obtained  $R_\tau = 0.997$  for  $N_{\text{points}} = 64119$ , which is again a reasonable value of  $R_\tau$ .

## 3.3. Calculated spectra

In this section, we compare the emergent spectra calculated from our simulations. Since spectral synthesis is our main goal in the development of new numerical models, it is essential that we verify the accuracy of spectra calculated from models with numerically interpolated velocity fields. Our focus will be on the previously discussed homologous approximation and the  $\beta$ -law. Model parameters are listed in Table 1 and are the same for both velocity fields.

### 3.3.1. Homologous approximation

We applied the equation of the homologous velocity field (9) and the corresponding optical depths (15) or (13) for the analytical and numerical case, respectively. The spectra and their relative differences for a homologous approximation are plotted in the

left panels of Fig. 4. The continua are in a good agreement. The largest difference is caused by noise. There are many spectral lines in the spectrum and there is no significant disagreement between them. Noise decreases with increasing wavelength and the largest differences occur in the emission profiles of the lines. Therefore the velocity interpolation is calculated correctly in the case of the homologous approximation.

### 3.3.2. $\beta$ -law

The spectra for the  $\beta$ -velocity law were calculated using both analytical (10) and numerical velocity fields, as well as the line optical depths using equations (16) and (13) for the analytical and numerical cases, respectively. The spectra are plotted in the right panels of Fig. 4.

The spectra agree over a wide range of wavelengths, similarly to the case of the homologous approximation, the main peaks lie in the emission parts of the lines and the continuum noise is low.

## 4. Radiative transfer solution for a 2-D hydrodynamic model

To complement the accuracy analysis presented in the previous sections, we demonstrate the calculation capabilities of our code by presenting a solution to the problem of radiative transfer for a structure generated by a 2-D hydrodynamic code.

### 4.1. Brief description of the radiation-hydrodynamics code MPI-AMRVAC

MPI-AMRVAC (Porth et al. 2014; Xia et al. 2018; Keppens et al. 2020, 2023) is a general-purpose multi-dimensional PDE-solver which has specialised itself in solving the time-dependent equations of (magneto-)hydrodynamics. (Moens et al. 2022b) developed a module to perform radiation-hydrodynamic computations in MPI-AMRVAC, making use of the flux-limited diffusion (FLD) formalism. This formalism requires the solution of the 0th order, frequency-integrated radiative transfer equation, where FLD offers an analytic closure relation between the radiative co-moving frame flux and the radiation energy density.

The addition of the radiation subsystem to the hydrodynamic equations allows for a more accurate treatment of both the source-terms in the momentum equation (radiative forces), and radiative source-terms in the energy equation (heating and cooling). Especially in a regime where the radiation field changes dynamically as an effect of a complex density structure.

The code solves the RHD equations using a finite volume approach for the advection terms, and a geometric multigrid solver (Teunissen & Keppens 2019) for the diffusive terms which are relevant for the FLD-closure. The finite volume solver works on an oct/quadtree grid with adaptive mesh refinement. Multiple Riemann solvers and timesteppers are available and described in Keppens et al. (2023).

Moens et al. (2022b) used the above described code to calculate a first set of multi-dimensional RHD models of WR atmospheres. For this, the RHD equations were solved in a local, box-in-wind Cartesian computational domain, where spherical corrections were added for the radial  $1/r^2$  factor in the divergence terms.

Later, Debnath et al. (2024) used the same setup to study the turbulent sub-photospheric regions in Ostars, ud-Doula et al.

(2025) and Narechania et al. (2025) continued this work by adding the effects of magnetic fields.

Important in the setup of these atmosphere and wind models is the calculation of the opacities. In the models used here, opacities are calculated as the sum of the Rosseland mean opacities, which are important in the deep atmosphere, and velocity-gradient enhanced opacities in the wind, making use of the Sobolev approximation. This so-called hybrid opacity scheme has been described by Poniatowski et al. (2021, 2022).

### 4.2. Implementation to the Andy Antares code

In this subsection, we describe how the input model was implemented in the code. When we implement a new model into the code, we have to test the following steps

- setting up the computational domain
- loading the input data
- transforming into Cartesian coordinates
- creating the propGrid (test whether it describes the input model correctly)

#### 4.2.1. Setting the computational domain, loading the input data

The input hydrodynamic model is two-dimensional, each point is defined by its radius,  $r$ , and its lateral coordinate,  $\vartheta$ . This model describes a 2-D part of the star, a ‘box in a wind’. The  $r$  coordinate describes the distance from the stellar centre. The model provides the mass density  $\rho$ , temperature  $T$ , and two components of the velocity field  $(v_r, v_\vartheta)$  in the  $r$  and  $\vartheta$  directions, respectively. To obtain a 3-D computational domain for radiative transfer calculations, we extend this ‘box in a wind’ model to describe the spherical star. First, we convert the 2-D rectangular model into an annular sector of lateral width  $\vartheta_{\max} = \pi/n$ , where  $n$  is a natural number. Then, we place  $n$  copies of this sector periodically side by side to form an annular sector of lateral length  $\pi$  within a plane intersecting the centre of the star. Finally, we rotate this annular sector around the  $z$ -axis to obtain the entire stellar envelope (a shell). For our calculations, we chose  $n = 4$ .

#### 4.2.2. Connection of propGrid with the model points

The velocity vector of the modGrid cell  $I$  is defined by its radial  $(v_r)_I$  and latitudinal  $(v_\vartheta)_I$  components, which must be evaluated for each propGrid cell centre  $J$  with position  $r_J$  and  $\vartheta_J$  and  $\varphi_J$  and the Cartesian components of this vectors are

$$\begin{pmatrix} v_x \\ v_y \\ v_z \end{pmatrix}_J = \begin{pmatrix} (v_r)_I \cdot \sin(\vartheta_J) \cdot \cos(\varphi_J) + (v_\vartheta)_I \cdot \cos(\vartheta_J) \cdot \cos(\varphi_J) \\ (v_r)_I \cdot \sin(\vartheta_J) \cdot \sin(\varphi_J) + (v_\vartheta)_I \cdot \cos(\vartheta_J) \cdot \sin(\varphi_J) \\ (v_r)_I \cdot \cos(\vartheta_J) + (v_\vartheta)_I \cdot \sin(\vartheta_J) \end{pmatrix}. \quad (17)$$

The MPI-AMRVAC model implemented was calculated in 2-D geometry, which brings a different treatment from the 1-D and 3-D cases. The model points are defined by radius ( $r$ ) and lateral coordinate ( $\vartheta$ ). We can get all the full information we need to calculate spectra. We load model points and for each point we get: radius, temperature, density, angular and lateral velocities. The next step is to set up the computational domain: the lower and the upper limits which are defined by the points with the smallest radius and largest radius. The propGrid is created, and each propGrid cell is assigned to a modGrid cell. Since we know

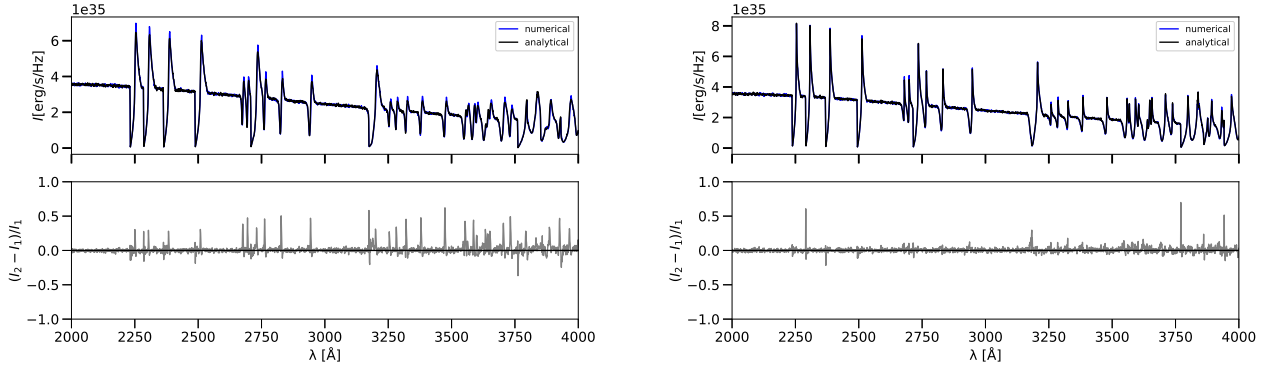


**Fig. 4.** A comparison of the calculated spectra for two models. In the first model the velocity (and line optical depth) was interpolated from the 3-D velocity points. In the second model the velocity (and line optical depth) was calculated using an analytical formula. *Left panels:* homologous approximation, *Right panels:*  $\beta$  velocity law

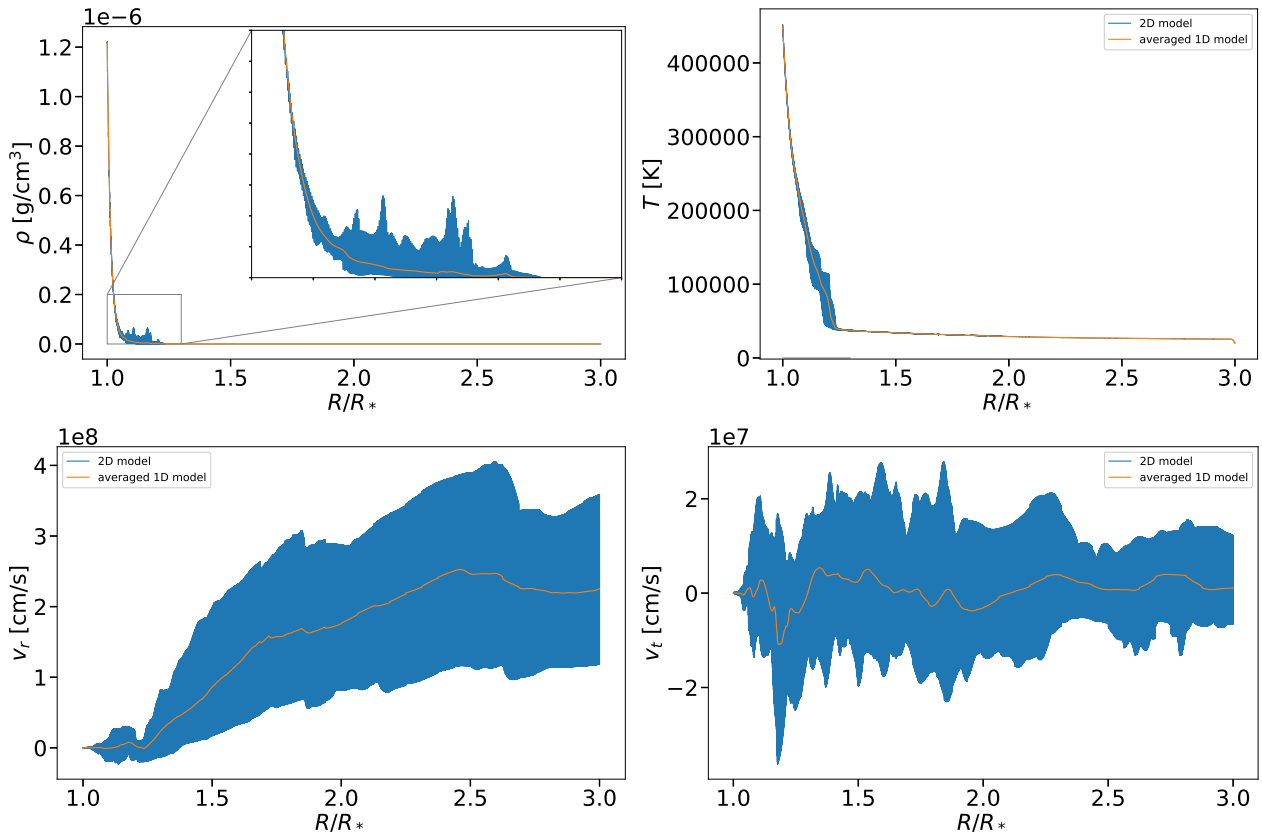


**Fig. 5.** The input model (density, temperature, and the radial and lateral velocities) calculated using the MPI-AMRVAC hydrodynamic code.

the cartesian coordinates, we calculate the lateral coordinates of each propGrid cell with a position  $\mathbf{r}_J = (x_J, y_J, z_J)$  as

$$r_J = \sqrt{x_J^2 + y_J^2 + z_J^2},$$

and lateral coordinates

$$\vartheta_J = \frac{z_J}{\sqrt{x_J^2 + y_J^2 + z_J^2}},$$

we can calculate the distance from a modGrid cell with coordinates  $r_I$  and  $\vartheta_I$  as

$$\delta = \sqrt{r_J^2 + r_I^2 - 2r_J \cdot r_I \cdot \cos(\vartheta_J - \vartheta_I)}, \quad (18)$$

we are seeking the modGrid cell with the shortest distance from the propGrid centre. We can run several tests to see if the propGrid we created accurately describes the modGrid. One important parameter is a relative coverage described in Paper I, Eq. (41), which describes a ratio of the number of modGrid cells that are connected to at least one propGrid cell to the total number of modGrid cells.

#### 4.3. Preliminary results of our simulations

The Tab. 2 contains important modGrid and propGrid parameters including the lower boundary conditions.

parameter	2-D	av. 1-D
lower boundary $R_*/R_\odot$	160	160
upper boundary $R_\infty/R_\odot$	480	480
$\theta_{\max}$	$\pi/4$	—
number of modGrid cells	1048576	2048
number of regular propGrid cells	$700 \times 700 \times 700$	$700 \times 700 \times 700$
number of propGrid cells	343 000 000	343 000 000
relative covering	40 %	100 %
number of packets	15 000 000	15 000 000
effective temperature [K]	30 000 or variable	

**Table 2.** Numerical parameters of the calculated model.

The distribution of density in the calculated model is depicted in Fig. 6. The grid is fine enough to resolute the included inhomogeneities.

We calculated the very first testing spectra of a homogeneous wind consisting of Hydrogen (73.46 %), Helium (24.85 %) and Carbon (0.29 %) by mass. To evaluate the importance of including of inhomogeneities, we created a 1-D model by averaging the physical quantities from the 2-D model in the lateral coordinates at each radial point, and solved radiation transfer for this 1-D model. Using the same geometric dimensions and the lower boundary conditions we calculated the spectrum emerging from the 1-D model and compared it with the 2-D model spectrum in Fig. 7. Naturally, the two spectra differ. The 1-D model, which is an average of the 2-D model, smooths the inhomogeneities in the medium, as it is depicted by the orange lines in Fig. 5. Consequently, it produces an emergent spectrum that differs from that emerging from the more exact 2-D input model. This highlights the importance of accurately resolving atmospheric inhomogeneities and including them in models. A similar conclusion was found for a simpler model by Tichý & Kubát (2019).

The figures (upper and lower) in the Fig. 7 differ in the lower boundary conditions. The upper spectrum was calculated for an assumption of Plank body radiation in the lower boundary ( $r = R_*$ ). The spectra below were calculated also for Plank distribution function in the lower boundary, but the effective temperature has been defined from the modGrid, hence the the distribution was depending also on the initial position of the packet.

## 5. Conclusions

We present a Monte Carlo radiative transfer code for the spectral synthesis. Our code is designed to calculate radiative transfer in multidimensional input models (2-D and 3-D) including general velocity fields (non-monotonic).

We have described the used numerical methods. The interaction in lines is simply generalised for non-monotonous velocity fields. In addition to the CMF redshift of a packet, the CMF blueshift is also included. The velocity field is linearly interpolated from the discrete points defined by the model. We performed interpolation tests using two simple velocity profiles: the homologous approximation (linear) and the  $\beta$ -law velocity profile. For each case, the interpolated velocity profile was compared with its analytical value. The differences become larger near the upper ( $r \approx R_*$ ) and the lower boundary ( $r \approx R_\infty$ ) limits. The middle parts of the velocity profiles are calculated with an error lower than 5 %. We compared the emergent spectra of all the velocity profiles. The spectra differ mainly in the emission parts of the lines, especially in the case of the homologous approximation. The continua fit well.

We adapted our code to compute the spectrum emerging from the 2-D hydrodynamic model MPI-AMRVAC, which is arranged in the form of a “box in the wind”. The implementation of the model in our code is described in Section 4.2. The main challenge lies in creating a propGrid that encompasses all the inhomogeneities, which requires the inclusion of each modGrid point in the propGrid. For our simulations, we created a regular propGrid and calculated the spectra. The spectrum of the 2-D model is compared with the spectrum of the 1-D model derived from the 2-D model by averaging quantities in the lateral coordinates. The two spectra differ significantly in terms of their line details, which highlights the importance of solving the problem using a multidimensional approach.

The 2-D model also introduces a new effect to packet propagation: in the case of monotonic velocity fields, red-shifting of the packet was the only possibility. In more complex velocity fields, blue-shifting of the packet is also possible. The effect of velocity fields with  $\frac{d\|v\|}{dr} < 0$  is usually neglected in the radiative transfer codes. However, it was straightforward to incorporate this effect into our code.

Radiative transfer is solved under several assumptions. The first limitation is the propGrid used. Although our code supports adaptive mesh refinement, we only used a regular grid here which reduced the number of used modGrid points used by the model to 40 %. However, it was still accurate enough to include inhomogeneities and clumping, as shown in Fig. 6. We compared the spectra calculated in the 2-D model and 1-D models with the averaged quantities from the 2-D model. The calculated spectra differ, mainly in the second case (the lower spectrum of Fig. 7). Therefore it is important to calculate 2-D and 3-D models. The differences would be more significant if spectra were calculated from a specific perspective, which has not yet been done.

*Acknowledgements.* JF was supported by the PPLZ programme of the Czech Academy of Sciences. Computational resources were supplied by the project “e-Infrastruktura CZ” (e-INFRA CZ LM2018140) supported by the Ministry of Education, Youth and Sports of the Czech Republic. JK and BK acknowledge support from the Grant Agency of the Czech Republic (GAČR 25-15910S). The Astronomical Institute of the Czech Academy of Sciences in Ondřejov is supported by the project RVO: 67985815.

*Special thanks from JF:* I would also like to thank a great teacher from my secondary school, Lumír Svoboda. He was a really brilliant teacher who motivated me to study maths and physics more intensively. I always recall those times at Elgartova School fondly.

## References

- Debnath, D., Sundqvist, J. O., Moens, N., et al. 2024, A&A, 684, A177
- Fišák, J., Kubát, J., Kubátová, B., Kromer, M., & Krtička, J. 2023, A&A, 670, A41
- Gräfener, G., Koesterke, L., & Hamann, W. R. 2002, A&A, 387, 244
- Hamann, W. R. & Gräfener, G. 2003, A&A, 410, 993

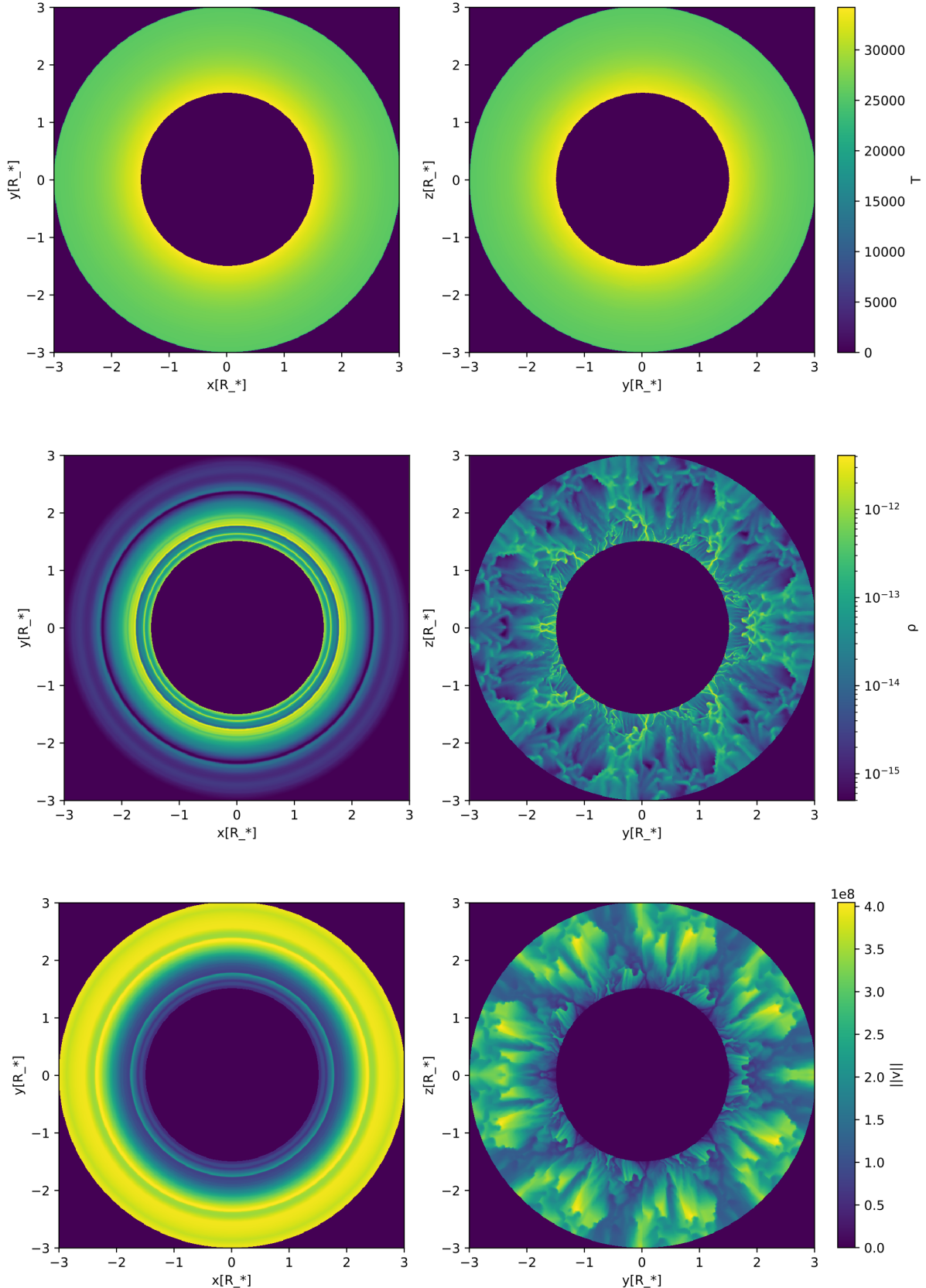


**Fig. 6.** Visualisation of the entire propGrid cut. A total of  $700 \times 700$  square cells are plotted in each figure. Each square represents one propGrid cell. The physical quantities are constant within the propGrid cell (except for the velocity field). **Columns:** *Left*:  $xy$  plane, the axis of symmetry is perpendicular to the plane of the plot, *right*:  $xz$  plane, the axis is parallel to the plane of the plot. **Rows:** 1. temperature, 2. density, 3. magnitude of velocity.

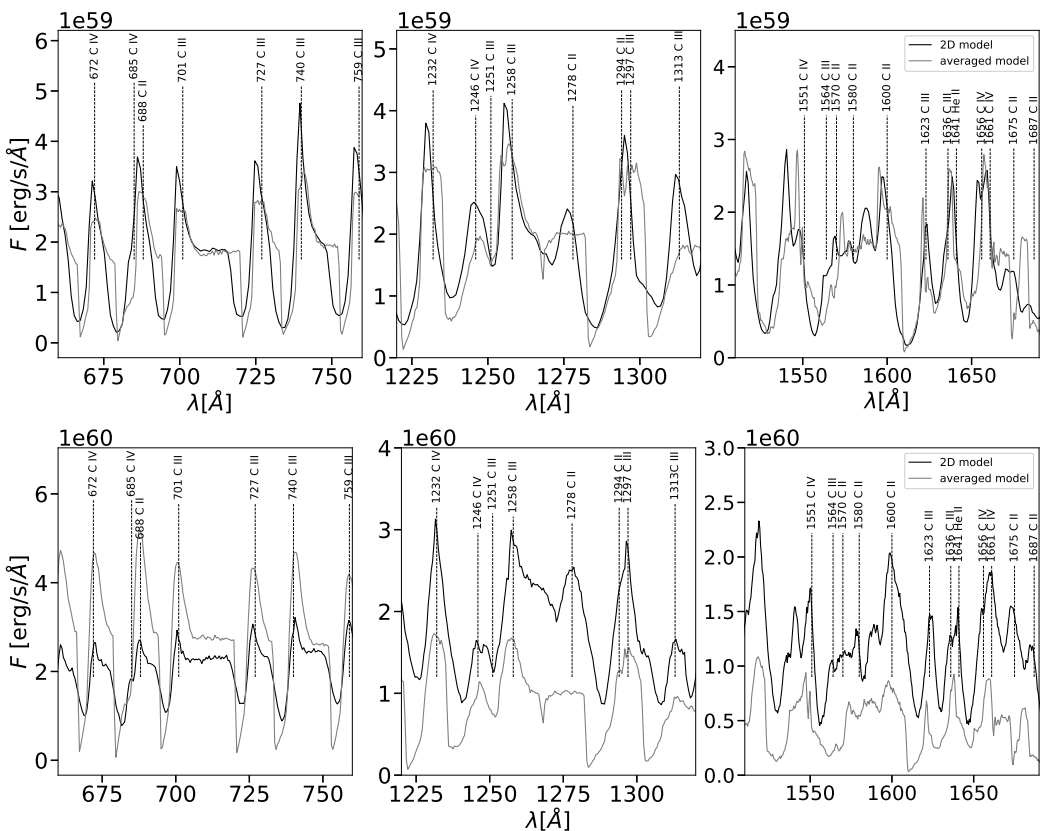


**Fig. 7.** Calculated spectra of two models from MPI-AMRVAC: 2-D and the same model averaged in  $\theta$ . The difference between upper and lower spectrum is the lower boundary effective temperature. *Above:*  $T_{\text{eff}} = 30000$  K, *below:* effective temperature is defined by the temperature of the initial packet point.

Higginbottom, N., Knigge, C., Long, K. S., Sim, S. A., & Matthews, J. H. 2013, MNRAS, 436, 1390  
 Keppens, R., Popescu Braileanu, B., Zhou, Y., et al. 2023, A&A, 673, A66  
 Keppens, R., Teunissen, J., Xia, C., & Porth, O. 2020, arXiv e-prints, arXiv:2004.03275  
 Kerzendorf, W., Sim, S., Vogl, C., et al. 2022, tardis-sn/tardis: TARDIS v2022.06.19  
 Kerzendorf, W. E. & Sim, S. A. 2014, MNRAS, 440, 387  
 Kromer, M. 2009, PhD thesis, Technische Universität München, München  
 Long, K. S. & Knigge, C. 2002, ApJ, 579, 725  
 Matthews, J. H., Long, K. S., Knigge, C., et al. 2025, MNRAS, 536, 879  
 Moens, N., Poniatowski, L. G., Hennicker, L., et al. 2022a, A&A, 665, A42  
 Moens, N., Sundqvist, J. O., El Mellah, I., et al. 2022b, A&A, 657, A81  
 Narechania, N., Keppens, R., ud-Doula, A., Moens, N., & Sundqvist, J. 2025, A&A, 696, A131  
 Poniatowski, L. G., Kee, N. D., Sundqvist, J. O., et al. 2022, A&A, 667, A113  
 Poniatowski, L. G., Sundqvist, J. O., Kee, N. D., et al. 2021, A&A, 647, A151  
 Porth, O., Xia, C., Hendrix, T., Moschou, S. P., & Keppens, R. 2014, ApJS, 214, 4  
 Press, W. H., Teukolsky, S. A., Vetterling, W. T., & Flannery, B. P. 1992, Numerical recipes in FORTRAN. The art of scientific computing (Press Syndicate of the University of Cambridge)  
 Sander, A., Shenar, T., Hainich, R., et al. 2015, A&A, 577, A13  
 Sander, A. A. C., Bouret, J. C., Bernini-Peron, M., et al. 2024, A&A, 689, A30  
 Teunissen, J. & Keppens, R. 2019, Computer Physics Communications, 245, 106866  
 Tichý, A. & Kubát, J. 2019, J. Quant. Spectr. Rad. Transf., 225, 249  
 ud-Doula, A., Sundqvist, J. O., Narechania, N., et al. 2025, A&A, 693, A224  
 Vogl, C., Sim, S. A., Noebauer, U. M., Kerzendorf, W. E., & Hillebrandt, W. 2019, A&A, 621, A29  
 Šurlan, B., Hamann, W. R., Aret, A., et al. 2013, A&A, 559, A130  
 Šurlan, B., Hamann, W. R., Kubát, J., Oskinova, L. M., & Feldmeier, A. 2012, A&A, 541, A37  
 Xia, C., Teunissen, J., El Mellah, I., Chané, E., & Keppens, R. 2018, ApJS, 234, 30

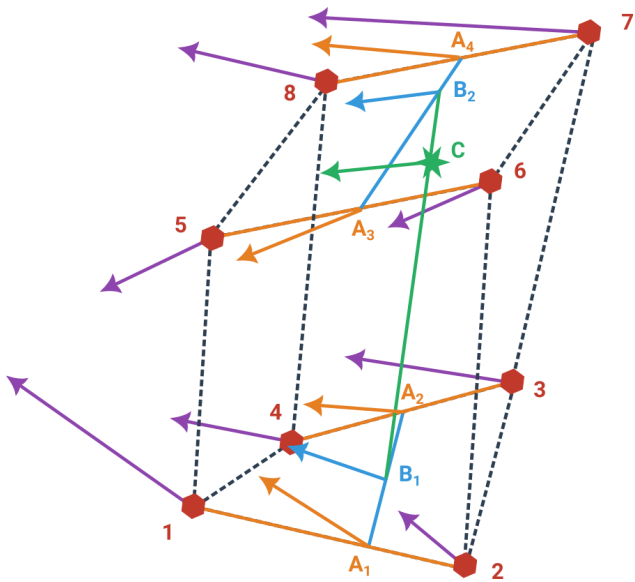


**Fig. A.1.** Scheme of the trilinear interpolation. We aim to determine the value at the green point (C). The interpolated physical quantity is defined in the eight red points placed in the red hexagonal. Using linear interpolations, new values are calculated in four orange points ( $A_1 \dots A_4$ ), using these orange points we obtain values in the blue points ( $B_1$ ,  $B_2$ ), and, finally, we calculate the value in the green point C.

## Appendix A: The trilinear interpolation

The trilinear interpolation consists of linear interpolations performed successively in three dimensions, it is described in Press et al. (1992) and depicted in Fig. A.1.

A non-trivial part is a determination, which propGrid cells are neighbouring the current cell and can be used for this algorithm. This calculation is described in the Section 2.3.1 and depicted in the Fig. 1. In the beginning, an octant of the propGrid cell where the value in the green point from Fig. A.1 is determined.

Let us assume two points:  $A_1$  and  $A_2$  at positions  $\mathbf{r}_1$  and  $\mathbf{r}_2$  containing velocity vectors  $\mathbf{v}_1$  and  $\mathbf{v}_2$ , respectively. We want to find a velocity vector at a specific point on a straight line between these two points  $A_1$  and  $A_2$ . The equation of the straight line is equal to

$$\mathbf{r}(\delta) = \mathbf{r}_1 + \frac{\mathbf{r}_2 - \mathbf{r}_1}{|\mathbf{r}_2 - \mathbf{r}_1|} \cdot \delta. \quad (\text{A.1})$$

Here,  $\delta$  is the parameter of the straight line (distance from the point  $\mathbf{r}_1$ ). Assuming the following conditions  $\mathbf{r}_1$ , it is  $\delta = 0$ , in the second point  $\delta = |\mathbf{r}_2 - \mathbf{r}_1| = d$ , we can write the interpolated velocity is in the form

$$\mathbf{v}(\delta) = \frac{\mathbf{v}_1 - \mathbf{v}_2}{d} \cdot \delta + \mathbf{v}_1. \quad (\text{A.2})$$

The value of the parameter  $\delta$  is obtained from the Eq. (A.1), where we put a selected coordinate ( $x$ ,  $y$ , or  $z$ ) calculated. The interpolation is independent of the order of this choice.

Neighbouring propGrid cells are chosen according to a relative position of the green point to the current propGrid centre – those propGrid cells have common bound, edge, or corner with the occupied octant of the current propGrid cell.